Optical depth measurements by shadow-band radiometers and their uncertainties

Mikhail D. Alexandrov,[1,2,*] Peter Kiedron,[3] Joseph J. Michalsky,[3] Gary Hodges,[3] Connor J. Flynn,[4] and Andrew A. Lacis[2]

[1]Department of Applied Physics and Applied Mathematics, Columbia University, New York, New York 10025, USA
[2]NASA Goddard Institute for Space Studies, 2880 Broadway, New York, New York 10025, USA
[3]NOAA Earth System Research Laboratory, R/GMD1, Boulder, Colorado 80305-3337, USA
[4]Pacific Northwest National Laboratory, P.O. Box 999, Richland, Washington 99352, USA

*Corresponding author: malexandrov@giss.nasa.gov

Received 3 July 2007; accepted 7 September 2007;
posted 12 September 2007 (Doc. ID 84807); published 15 November 2007

Shadow-band radiometers in general, and especially the Multi-Filter Rotating Shadow-band Radiometer (MFRSR), are widely used for atmospheric optical depth measurements. The major programs running MFRSR networks in the United States include the Department of Energy Atmospheric Radiation Measurement (ARM) Program, U.S. Department of Agriculture UV-B Monitoring and Research Program, National Oceanic and Atmospheric Administration Surface Radiation (SURFRAD) Network, and NASA Solar Irradiance Research Network (SIRN). We discuss a number of technical issues specific to shadow-band radiometers and their impact on the optical depth measurements. These problems include instrument tilt and misalignment, as well as some data processing artifacts. Techniques for data evaluation and automatic detection of some of these problems are described.

OCIS codes: 120.4640, 120.5240, 120.5630, 120.0280, 010.1100, 010.1120.

1. Introduction

Aerosol optical depth (AOD) is the most basic, and perhaps most important product of Sun-photometric measurements. [According to the American Meteorological Society (AMS) Glossary of Meteorology, optical thickness gives the line integral of extinction along any line of sight (e.g., Sun photometer to the Sun), while optical depth (OD) is optical thickness projected onto a vertical path. This definition is consistent with terminology used by the World Meteorological Organization (WMO) Guide to Meteorological Instruments and Methods of Observation.] The main source of uncertainties in AOD measurements is instrument calibration, which, for example, limits the accuracy of AOD derived from Aerosol Robotic Network (AERONET) CIMEL tracking Sun photometer data to ± 0.01 for wavelengths longer than 440 nm, and ± 0.02 for shorter wavelengths [1]. Calibration accuracy of the Multi-Filter Rotating Shadow-band Radiometer (MFRSR, cf. [2]) achievable through a long-term Langley analysis is essentially the same: 0.01 in OD [3]. Like the tracking Sun photometers, shadow-band instruments have some specific accuracy issues in addition to calibration uncertainties. The problems affecting MFRSR (and its more sophisticated relative Rotating Shadow-band Spectroradiometer (RSS) [4,5]) involve instrument alignment, tilt, and accuracy of angular response determination [6]. In this study we will estimate the errors in AOD caused by some of these problems and suggest some techniques to identify and quantify them.

We will illustrate the above mentioned effects using data from the vast MFRSR dataset from the local network at the U.S. Southern Great Plains (SGP) run by the Department of Energy (DOE) Atmospheric Measurement (ARM) Program [7]. This network consists of 21 instruments located at the SGP Central (CF) and Extended Facilities (EF), and covers an area of approximately $3° \times 4°$ in northern Oklahoma and southern Kansas with average spacing of 80 km between neighboring measurement sites. Other major networks operating MFRSRs in the United States are

0003-6935/07/338027-12$15.00/0

the U.S. Department of Agriculture (USDA) UV-B Monitoring and Research Program [8], National Oceanic and Atmospheric Administration (NOAA) Surface Radiation (SURFRAD) Network [9], and NASA Solar Irradiance Research Network (SIRN). Internationally MFRSRs are operated mostly by individual users. However, many stations of the World Climate Research Programme (WCRP) Baseline Surface Radiation Network (BSRN) [10], and Australian Bureau of Meteorology Solar and Terrestrial Network [11] are equipped with these instruments.

2. Optical Depth Measurements

A. Shadow-Banding Technique

The MFRSR makes precise simultaneous measurements of the solar irradiances at six wavelengths (nominally 415, 500, 615, 673, 870, and 940 nm) at short intervals (20 s for ARM instruments) throughout the day. Time series of direct solar beam extinctions and horizontal diffuse fluxes are derived from the four actual measurements made at each data point. From the modeling point of view each of the measurements is essentially the Sun–sky irradiance integrated over the unblocked part of the sky. This integration is weighted with the instrument's angle- and wavelength-dependent responsivity. The four measurements are S_{toth}, which is the total horizontal irradiance with the shadow band located under the diffuser not blocking any light; S_{blk}, which is the Sun-blocked measurement; and two side band measurements, S_{se} and S_{sw}, with shadow-band blocking a section of the sky 9° east and west, respectively, from the Sun. The two side measurements are averaged,

$$S_s = \frac{S_{sw} + S_{se}}{2}, \tag{1}$$

and used to estimate the solar aureole contribution in the blocked measurement,

$$S_{aur} = S_{toth} - S_s, \tag{2}$$

which should be added to the blocked measurement to determine the diffuse irradiance. We should note that, while aureole intensity is peaked in the Sun direction, the value obtained from Eq. (2) is always an underestimation. However, the influence of this effect is negligible unless the effective aerosol particle radius is really large (exceeding 1 μm). A correction for the "shadow-banding error" may be needed, e.g., for dust storm events, and especially for an estimation of the OD of thin clouds [12]. A technical solution for this problem may be an increase in the number of side measurements by at least one from each side, or by programming the shadow band to rotate continuously, as suggested in [13]. Detailed analysis of the errors due to shadow banding will be a subject of a separate study.

The described four measurements are combined (currently by the instrument's data logger) into the diffuse horizontal,

$$S_{difh} = S_{blk} + S_{aur} = S_{blk} + S_{toth} - S_s, \tag{3}$$

and direct horizontal,

$$S_{dirh} = S_{toth} - S_{difh} = S_s - S_{blk}, \tag{4}$$

measurements. The latter is normalized

$$S_{dir} = \frac{S_{dirh}}{\cos\theta} \tag{5}$$

(θ is the solar zenith angle). The MFRSR data logger allows us to either record the measurements directly as they are made or instead provide the averages over several samples. For example, the MFRSRs operated by ARM Program provide samples every 20 s with no averaging, while SURFRAD Network instruments make measurements every 15 s and reported 2 min averages. If the measurements are being averaged, the normalization (5) is performed inside the instrument's data logger, while in the direct mode it is done after the data are downloaded to a computer. The latter is preferable because the rough 16 bit computations of θ in the logger add noise to the data. After normalization, S_{dir} is converted by the data unpacking software into the direct normal irradiance:

$$I = I_{dir} = \frac{1}{\tilde{C}} \frac{S_{dir}}{1 + \tilde{\eta}(\theta, \varphi)}, \tag{6}$$

where θ and φ are, respectively, the calculated (nominal) solar zenith angle and the solar azimuth. $\tilde{C}$ is the estimate of the instrument's total responsivity C (inverse of the calibration constant). It is measured in the laboratory or determined from the data by, e.g., Langley analysis. $[1 + \tilde{\eta}(\theta, \varphi)]$ with $|\tilde{\eta}(\theta, \varphi)| \ll 1$ is the estimate of the instrument's angular response ("cosine correction") function $[1 + \eta(\theta, \varphi)]$. $\tilde{\eta}$ is measured in the laboratory, and is normalized to unity at $\theta = 0°$.

B. Measurement Errors in Optical Depth

In the ideal situation where the measured signal is free from instrumental noise and the actual instrument's total and angular responsivities are precisely known, the direct normal irradiance can be represented as

$$I = I_0 \exp\left(-\frac{\tau}{\mu}\right), \tag{7}$$

where I_0 is top of atmosphere (TOA) irradiance, τ is optical depth, and μ is the inverse airmass [14] ($\mu \approx \cos\theta$ for small to moderate solar zenith angles). If I_0 is accurately known, the optical depth can be

derived from the direct normal irradiance:

$$\tau = -\ln\left(\frac{I}{I_0}\right)\mu. \quad (8)$$

However, in practice, measurements contain random noise, the characterization of instrument responsivity may be imperfect, and the instrument itself may be tilted. While the TOA spectrum may also contain uncertainties [15], they can be formally neglected if we are interested only in OD determination. Indeed, as it follows from Eqs. (6) and (8), I_0 and the instrument's responsivity C enter the expression for τ only as their product, thus the derived OD would not be altered if we assign the errors in both these constants to C, assuming that I_0 is known precisely. Actually, in the traditional Langley analysis terminology the two constants are combined into one "extrapolated zero-airmass irradiance" (usually also called I_0) [16].

The measured S_{dirh} can be expressed in terms of atmospheric parameters and actual instrument characteristics as

$$S_{dirh} = I_0 C[1 + \eta(\theta', \varphi')]\cos\theta' \exp\left(-\frac{\tau}{\mu}\right) + e_0, \quad (9)$$

where e_0 is random noise (e.g., digitization), and θ' and φ' are the effective solar angles, which may be different from the nominal θ and φ if the instrument is tilted. Note that μ is not changed by tilt, since the light path in the atmosphere remains the same. The "real life" estimate $\tilde{\tau}$ of the actual OD τ is derived according to Eqs. (5), (6), and (8) using the instrument responsivity estimates $\tilde{C}$ and $\tilde{\eta}$, determined in the laboratory or from the data, together with the nominal solar angles. Assuming that $e_0 \ll S_{dirh}$ [that allows us to use $\ln(1 + x) \approx x$], we can express this estimate as follows:

$$\tilde{\tau} = \tau + \tau_{cal} + \tau_{cos} + \tau_{tilt} + \tau_{noise}, \quad (10)$$

where

$$\tau_{cal} = c\mu, \quad \text{where} \quad c = -\ln\left(\frac{C}{\tilde{C}}\right) \quad (11)$$

is the calibration error due to uncertainty in the instrument's total responsivity;

$$\tau_{cos} = -\mu \ln\left[\frac{1 + \eta(\theta, \varphi)}{1 + \tilde{\eta}(\theta, \varphi)}\right] \approx \mu[\tilde{\eta}(\theta, \varphi) - \eta(\theta, \varphi)] \quad (12)$$

is the error due to uncertainty in the angular response function (the last equality uses $\eta \ll 1$);

$$\tau_{tilt} = \tau_{tilt}^{(n)} + \tau_{tilt}^{(c)} \quad (13)$$

is the error due to the instrument's tilt consisting of two parts,

$$\tau_{tilt}^{(n)} = -\mu \ln\left(\frac{\cos\theta'}{\cos\theta}\right), \quad (14)$$

which is introduced in the normalization step (5), and

$$\tau_{tilt}^{(c)} = -\mu \ln\left[\frac{1 + \eta(\theta', \varphi')}{1 + \eta(\theta, \varphi)}\right] \approx \mu[\eta(\theta, \varphi) - \eta(\theta', \varphi')], \quad (15)$$

which is introduced when the correction for the instrument's angular response (6) is applied (here η can be replaced with $\tilde{\eta}$ for estimation purposes). The last term in Eq. (10),

$$\tau_{noise} = -\mu \frac{e_0}{S_{dirh}} \approx -\frac{e_0}{S_{dir}}, \quad (16)$$

is the instrument noise propagated to OD (the last equality implies $\mu \approx \cos\theta'$). This expression indicates an increase in random noise at low Sun elevations (early morning and late afternoon), and/or high optical depths.

C. Angular Response Functions

The angular response of shadow-band radiometers is characterized by laboratory measurements in south–north and west–east directions for all spectral channels [17]. Multiple measurements of the same responses are usually averaged to reduce noise. An example of the resulting "cosine correction" function is presented in Fig. 1 (top panels). The characteristic features at large angles there result from the sharp edges of the cylinder-shaped MFRSR diffuser. These functions are supplied to users with the instrument, and are applied to direct normal measurements by the data unpacking software. Linear interpolation between south–north and west–east functions is used to obtain angular correction at specific solar zenith and azimuth angles.

While the accuracy of laboratory angular calibration is hard to quantify, we may estimate the impact of gradual changes in the instrument's angular response on OD measurements. These changes are usually slow and are likely to be attributed to degradation of the diffuser material due to, e.g., soiling [8]. Currently routine angular characterization of MFRSRs deployed at the SGP site is not being performed due to the lack of spare heads. However, we obtained (courtesy of John Schmelzer) historic angular response measurements performed from 2002 to 2006 for two MFRSR heads (MP923 and MP924) from the North Slope of Alaska (NSA) ARM site. The MP923 head responses exhibited large differences between the measurements made at different times, and the last two measurements made in December 2006 showed completely unacceptable shapes of 500 nm response functions. This suggested that this head was probably originally faulty, and the

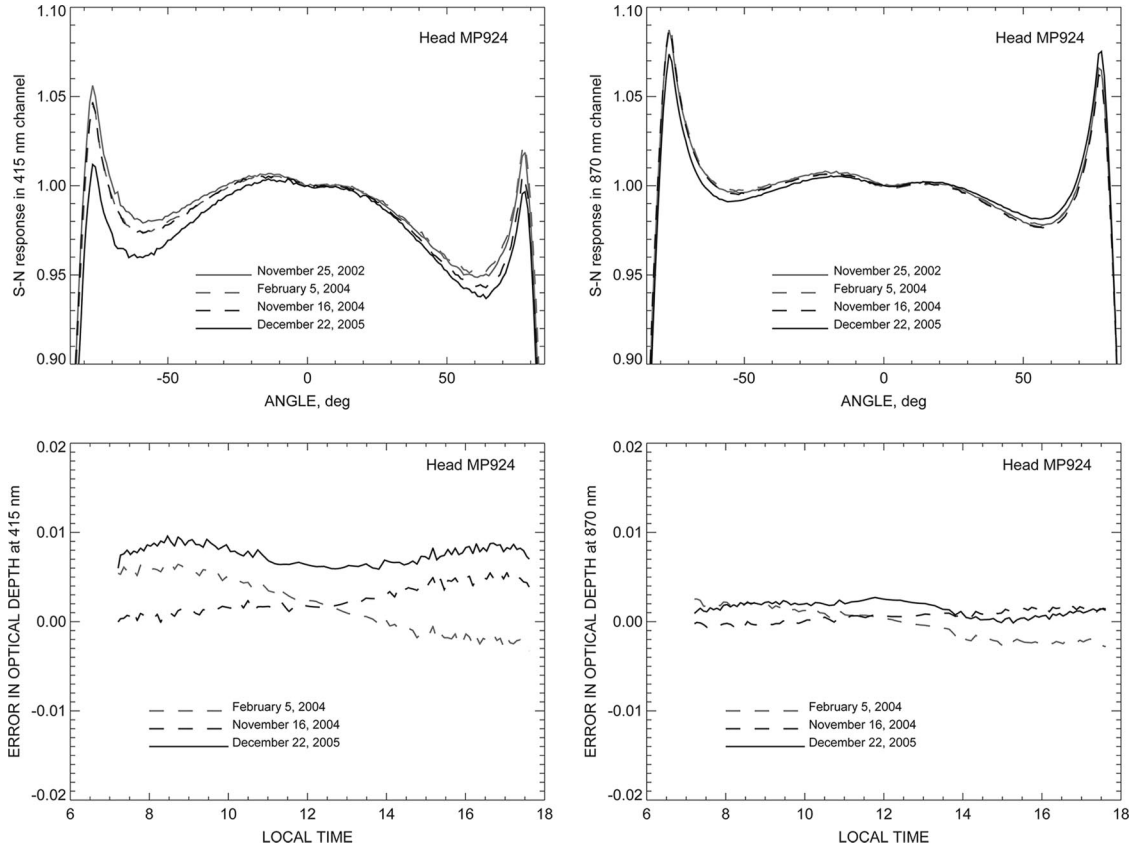

Fig. 1. Top: historic measurements of 415 and 870 nm angular responses in the south–north direction for the head MP924. Bottom: errors in 415 and 870 nm OD introduced by applying the 25 November 2002 response instead of the more recent ones. The errors are calculated for the solar geometry of SGP's Central Facility on 16 September 2000.

data obtained with it should be examined with caution. This underlines the importance of regular monitoring of MFRSR heads. The angular responses of the other head MP924 appeared to be substantially more stable, thus, characteristic of a normal "healthy" head. Figure 1 (top panels) shows the 415 and 870 nm angular responses in south–north direction for this head measured on 25 November 2002, 5 February 2004, 16 November 2004, and 22 December 2005 (the response functions in the west–east directions, and/or in other channels are similar).

We use Eq. (12) to evaluate the influence of angular response changes on OD measurements. To do this we assume that the only laboratory-measured cosine correction ($\tilde{\eta}$) available to us is that of 25 November 2002, while the rest of the measurements present the actual head responses (η). The bottom panels of Fig. 1 show the corresponding errors in 415 and 870 nm ODs calculated for the solar geometry of SGP's Central Facility on 16 September 2000. The errors appear to be larger in the 415 nm channel, however, for all six MFRSR spectral channels they are smaller than the calibration accuracy of 0.01. We should note from these plots that the time series of cosine correction errors may be quite different from those of calibration ($\propto \mu$) and, therefore, they cannot be corrected by Langley regressions.

D. Influence of Instrument Tilts

Instrument tilt is often a source of measurement errors for shadow-band Sun photometers. A severe tilt in the west–east direction can result in a sharp artificial spike in the direct irradiance plot in early morning or late afternoon (it is best seen in the 870 nm channel). Smaller tilts are more difficult to detect from the data. As we demonstrated above, the tilt influences the optical depth measurements in two ways. The first, and strongest effect occurs at the step of normalization of the direct horizontal measurement (5), since S_{dirh} is divided by the cosine of the nominal solar zenith angle θ instead of the actual θ'. This results in an artificial OD (14). Since tilt can be characterized by zenith and azimuth angles θ_t and φ_t, we can express $\cos\theta'$ in Eq. (14) as

$$\cos\theta' = \cos\theta\cos\theta_t + \sin\theta\sin\theta_t\cos(\varphi - \varphi_t) \tag{17}$$

$$\approx \cos\theta + \sin\theta\cos(\varphi - \varphi_t)\theta_t. \tag{18}$$

In Eq. (18) we assumed that $\theta_t \ll 1$. After this the expression (14) takes the following form:

$$\tau_{tilt}^{(n)} = -\ln[\cos\theta_t + \tan\theta\sin\theta_t\cos(\varphi - \varphi_t)]\mu. \tag{19}$$

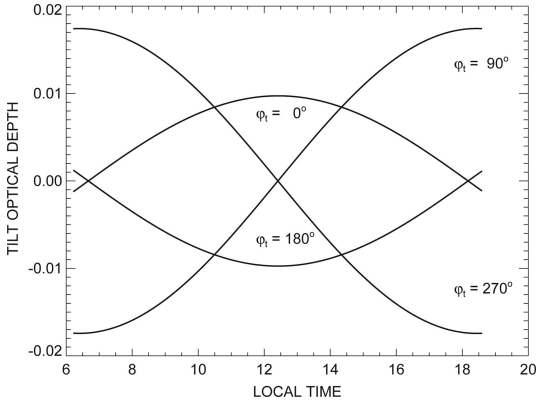

Fig. 2. Artificial additions to measured OD due to 1° tilts of MFRSR in different directions.

Assuming, that θ_t is small, we use $\sin\theta_t \approx \theta_t$, $\cos\theta_t \approx 1$, and also $\mu \approx \cos\theta$, and we can write Eq. (13) in much simpler approximate form:

$$\tau_{tilt}^{(n)} \approx -\sin\theta\cos(\varphi - \varphi_t)\theta_t. \tag{20}$$

The differences between the exact and the approximate formulas start to show up only at airmasses exceeding ten, which are not practical for OD measurements. Up to that airmass the differences are under 0.0035 (the largest are for west–east tilts). The results obtained using the approximate relation (20) are presented in Fig. 2. The solar angles here are calculated for 16 September 2000 at SGP Central Facility: 36.61 °N, 97.49 °W. We see that a modest tilt of 1° may produce wavelength-independent errors in OD up to 0.02. Contributions of tilts larger or smaller than 1° are easy to estimate, since Eq. (20) is linear in θ_t. It is also shown in Fig. 2, that while the tilts in the south or north directions create a contribution similar to those of calibration (const μ) and may be in part corrected by, e.g., the Langley calibration procedure, the tilts in west–east direction introduce artificial trends throughout the day. These trends decrease the reliability of Langley regressions by introducing a difference between morning and afternoon calibrations.

The direction and magnitude of the MFRSR tilt can be estimated in some cases by comparison with a colocated tracking Sun photometer (e.g., CIMEL), which is not susceptible to tilt issues. The same technique can be used for two shadow-band instruments (MFRSR or RSS), however, in this case both instruments may be tilted; thus we can estimate only the relative tilt. Here we neglect the second much smaller component (15) of $\tau_{tilt} \approx \tau_{tilt}^{(n)}$. The compared instruments may have a calibration difference in retrieved OD. To eliminate it we derive τ_{tilt} from a Langley-type regression on the difference between the ODs from the two instruments. Note that we need the whole clear day for this analysis. This procedure may eliminate a large part of tilt OD as well, if the tilt is in south–north direction. Thus, this procedure is limited mostly to an estimation of west–east direction tilts, which actually affect data the most. Once τ_{tilt} is obtained, we can use Eq. (20) with known θ and φ to estimate θ_t and φ_t. Equation (20) can be rewritten in the following form:

$$-\frac{\tau_{tilt}}{\sin\theta\cos\varphi} \approx A\tan\varphi + B, \tag{21}$$

where

$$A = \theta_t\sin\varphi_t, \qquad B = \theta_t\cos\varphi_t \tag{22}$$

are constants, which can be determined from the regression of Eq. (21) in $\tan\varphi$. Then we derive the tilt angles as

$$\varphi_t = \arctan\left(\frac{A}{B}\right), \qquad \theta_t = \sqrt{A^2 + B^2}. \tag{23}$$

To illustrate this we took daily 870 nm OD (AOD) time series from C1 and E13 MFRSRs located at SGP's Central Facility and from the colocated AERONET CIMEL ("Cart_Site") for 16 September 2000. The resulting τ_{tilt} time series (sampled at CIMEL data points) are shown in Fig. 3. While the plots for both MFRSRs exhibit some variability, likely due to uncertainties in the instrument's angular responses, they still can be used to estimate the tilt parameters.

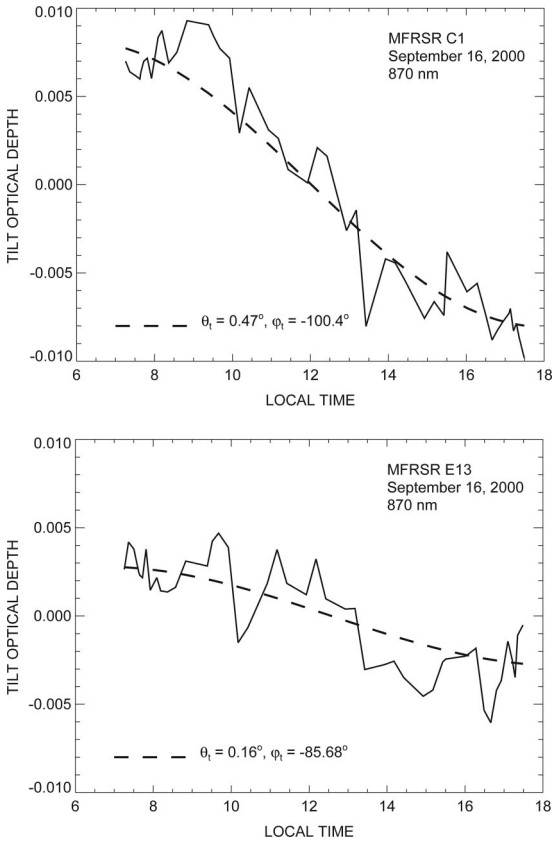

Fig. 3. Artificial addition to C1 and E13 MFRSR OD in 870 nm channel derived from comparison with colocated tracking CIMEL Sun photometer. The data is from 16 September 2000. All three instruments are located at SGP's Central Facility.

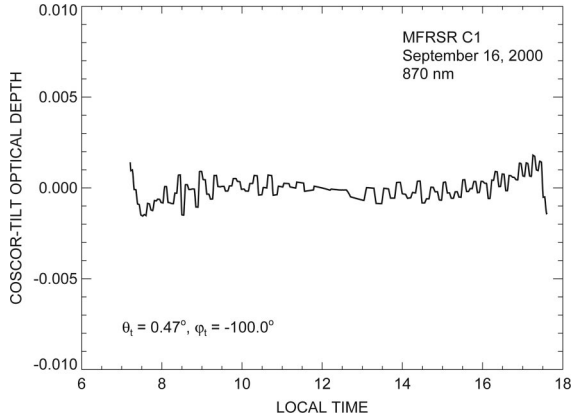

Fig. 4. Error in 870 nm OD due to the second (cosine correction) tilt effect simulated according to Eq. (15) for C1 MFRSR using its actual angular response function and the tilt parameters from Fig. 3 (top).

We see that both MFRSRs were tilted westward during this day: E13 was tilted only slightly by 0.16°, while C1 was tilted by a larger 0.47° angle. Certainly, the instrument's tilt estimation accuracy is not as good as 0.01°; the same estimates based on 673 nm AODs produce close, but different, tilt angles: $\theta_t = 0.30°$, $\varphi_t = -88.22°$ for E13, $\theta_t = 0.64°$, and $\varphi_t = -96.44°$ for C1. Thus, the accuracy of tilt estimation is at best 0.2° for θ_t and a few degrees for φ_t.

The second effect of tilt on OD retrievals is due to an inadequate angular correction of the measurements made by a tilted instrument. For west–east tilts this effect is an order of magnitude weaker than the normalization effect described above, as it can be seen from comparing Figs. 3 (top) and 4. The latter plot shows the error in OD due to the second tilt effect simulated according to Eq. (15) for C1 MFRSR using the actual angular response function and the tilt parameters from Fig. 3 (top). For moderate south–north tilts the second effect may be comparable to the first, however, in these cases both effects can be substantially reduced by calibration procedures. In an extreme situation of an unusually large (e.g., 4°) tilt in the south–north direction the second tilt effect can be seen more clearly. In this case the part of the tilt OD proportional to μ (mostly due to the normalization effect) is removed by the calibration procedure, and the second tilt effect shows up in the form of artificial oscillations in the OD reflecting features in the wings of the instrument's angular response function [Fig. 1 (top panels)]. These oscillations look quite different from the misalignment signature described below, and do not change the mean OD values. This situation is very rare and the authors can recollect only one case. It involved the ARM-operated E13 MFRSR and occurred in early April 2000 (5 April is a good example). Since the tilt was so severe, it was detected and fixed within a week.

E. Artificial Offsets in Direct Normal Irradiances

It had been discovered recently (December 2005) that the MFRSR manufacturer's data processing software has a "bug": the direct normal irradiances were erroneously corrected for the nighttime offsets (dark counts). Moreover, the offset correction was applied after the normalization (5). The offsets are characteristic of any instrument (currently determined by laboratory measurements), and are present in all four actual measurements described in Subsection 2.A. The stability of laboratory-measured offset characterizations is uncertain, thus actual field measurements at night would be a better alternative. Regardless of the offset accuracy, the direct horizontal, as it follows from Eq. (4), is a difference measurement, thus the offsets present in I_s and I_{blk} cancel. If the erroneously applied offsets are positive, they can be reconstructed from direct normal measurements made in the absence of direct sunlight, i.e., on a completely overcast day or during short intervals at dawn and dusk (the MFRSR starts reporting data when the onboard ephemeris calculates a solar zenith angle of less than 90° and reports the direct normal as zero until the Sun is 1° above the horizon). This zero turns into the total offset (applied, not actual) after data unpacking. The offsets are usually small, however, as we will show below, in some cases they may cause a notable error in the OD. For example, the offsets observed in the calibrated direct normal irradiances from C1 MFRSR at the dawn of September 2005 were 0.0167, 0.0081, 0.0035, 0.0026, and 0.0013 in 415, 500, 615, 673, and 870 nm channels, respectively. These values seem to be typical; the corresponding offset values obtained directly from the calibration file produced by Yankee Environmental Systems (YES) Inc. for a head with serial number 372 (chosen at random) are 0.0162, 0.0086, 0.0055, 0.0095, 0.0021, and 0.0016 (the last is for the 940 nm channel). The indication of the offset problem can be found in the manufacturer-supplied calibration file (usually with the ".cal" suffix) as the following piece of code:

```
# MFR direct normal
OUT(4, 4) := (DATA(0, 15) − (C0B*C0C) − C0D)/
  (C0A*C0C) ; # in W/m^2
OUT(4, 4) := (DATA(0, 16) − (C1B*C1C) − C1D)/
  (C1A*C1C) ; # in W/m^2 nm
OUT(4, 4) := (DATA(0, 17) − (C2B*C2C) − C2D)/
  (C2A*C2C) ; # in W/m^2 nm
OUT(4, 4) := (DATA(0, 18) − (C3B*C3C) − C3D)/
  (C3A*C3C) ; # in W/m^2 nm
OUT(4, 4) := (DATA(0, 19) − (C4B*C4C) − C4D)/
  (C4A*C4C) ; # in W/m^2 nm
OUT(4, 4) := (DATA(0, 20) − (C5B*C5C) − C5D)/
  (C5A*C5C) ; # in W/m^2 nm
OUT(4, 4) := (DATA(0, 21) − (C6B*C6C) − C6D)/
  (C6A*C6C) ; # in W/m^2 nm
```

instead of the correct

MFR direct normal

OUT(4, 4) := DATA(0, 15)/(C0A*C0C) ; # in W/m^2

OUT(4, 4) := DATA(0, 16)/(C1A*C1C) ; # in W/m^2 nm

OUT(4, 4) := DATA(0, 17)/(C2A*C2C) ; # in W/m^2 nm

OUT(4, 4) := DATA(0, 18)/(C3A*C3C) ; # in W/m^2 nm

OUT(4, 4) := DATA(0, 19)/(C4A*C4C) ; # in W/m^2 nm

OUT(4, 4) := DATA(0, 20)/(C5A*C5C) ; # in W/m^2 nm

OUT(4, 4) := DATA(0, 21)/(C6A*C6C) ; # in W/m^2 nm

Assuming that the instrument is perfectly calibrated and has no other problems (e.g., tilt), we can write the analog of Eq. (7) for this case as

$$I = I_0 \exp\left(-\frac{\tau}{\mu}\right) + e_{OF}, \tag{24}$$

where $e_{OF} \ll I$ is the offset value. The estimate of the OD from Eq. (24) is

$$\tilde{\tau} = \tau - \tau_{OF}, \tag{25}$$

where τ is the actual OD and

$$\tau_{OF} \approx \frac{e_{OF}}{I}\,\mu \approx \frac{e_{OF}}{I_0}\,\mu \exp\left(\frac{\tau}{\mu}\right) \tag{26}$$

is the artificial "offset OD" caused by e_{OF}.

We see from Eq. (26) that the magnitude of τ_{OF} depends exponentially on the total OD (including Rayleigh and ozone). This indicates that the 415 nm channel is expected to be affected the most, since it has the largest OD (with strong contributions from both Rayleigh and fine mode aerosol), the largest offsets, and I_0 smaller than in the next 500 nm channel. Figure 5 presents quantitative estimates of τ_{OF} simulated at MFRSR wavelengths according to Eq. (26) for the above mentioned offsets for head 372. The actual ODs were simulated using the atmospheric parameters typical for SGP's CF: 870 nm AOD of 0.1 split in half between the fine ($r_{\text{eff}} = 0.15$ μm) and coarse ($r_{\text{eff}} = 1.5$ μm) modes, ozone column of 300 DU, and Rayleigh OD corresponding to 980 mb ground pressure. The total OD at 415 nm is 0.6 for these parameters. The airmass values were computed for 16 September 2000 at SGP's CF. Only the values corresponding to airmasses less than 5 are shown in the figure, since the data at larger airmasses are not suitable for retrievals anyway (due to, e.g., uncertainties in MFRSR's angular response at large solar zenith angles). As expected, we see from Fig. 5 that while the values of τ_{OF} in 500–870 nm channels are practically negligible, compared to the measurement accuracy, the 415 nm τ_{OF} is substantially higher, especially at large airmasses [due to the factor $\exp(\tau/\mu)$ in Eq. (26)]. In the worst case of the OD 0.2 at 870 nm (the maximum for SGP's CF in, e.g., 2000), the corresponding 415 nm OD is 0.9, and the value of τ_{OF} at 415 nm becomes 0.023 at noon, and as large as 0.17 at airmass 5. However, such abnormal behavior has never been observed in real SGP data. We can conclude that, while the bug in the data processing scheme must be fixed in any case, the errors in the measured OD induced by the erroneous offsets are smaller or comparable to the calibration accuracy under atmospheric conditions typical for the SGP. That is, these errors, though certainly recognizable, especially in the 415 nm channel, are tolerable. This, however, is not true for datasets from high AOD regions affected by industrial pollution and/or dust storms. In these cases the fraction by which AOD is reduced due to the offset bug (that is larger at shorter wavelengths than at longer ones) may cause a serious bias in the Angstrom exponent and an overestimation of aerosol particle size.

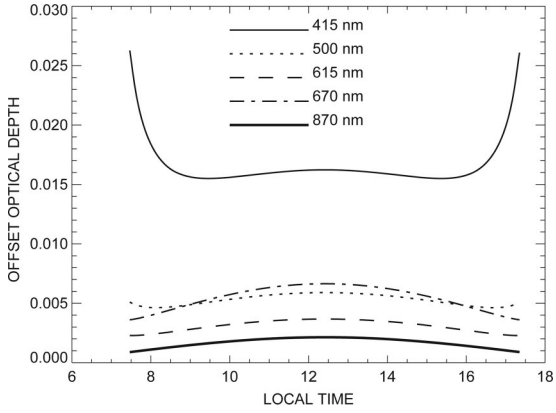

Fig. 5. Simulated artificial additional ODs caused by erroneous nighttime offset correction applied to direct normal irradiances. The calculations were made for solar geometry corresponding to 16 September 2000 at SGP's CF. The 870 nm AOD is 0.1 split in half between the fine and coarse modes, which have the respective r_{eff} of 0.15 and 1.5 μm. Only the values corresponding to airmasses less than 5 are shown.

F. Variation of MFRSR Channel Bandpasses

Current laboratory measurements of MFRSR spectral response functions are often inadequate. Moreover, large MFRSR networks (ARM, USDA UV-B Program) frequently exchange heads between their instruments, so it is sometimes hard to determine which head was installed on a particular instrument on a given day. However, a comparison (shown in Table 1) between parameters that is derived from spectral responses of a set of 44 heads (manufactured either by Battelle or Yankee Environmental Systems, Inc.) shows relatively little difference (2–6 nm) in effective wavelengths, which results in practically negligible differences in the OD of Rayleigh, NO_2, and ozone, which need to be subtracted from the extinction data to obtain spectral AOD. This fact, likely due to relatively wide MFRSR FWHM, means that accurate retrievals can be made even with nominal spectral parameters, with the exception, perhaps, of water vapor column estimates from 940 nm channel measurements.

We should emphasize, however, that if one attempts to retrieve the ozone column from MFRSR data, inaccurately measured (or taken from a wrong

Table 1. Statistics of Channels' Effective Wavelengths and Optical Depths of Rayleigh, NO_2, and Ozone (at Typical Atmospheric Conditions) Compiled from a Set of Spectral Response Functions for 44 Instrument Heads

Channel Nominal Wavelength (nm)	415	500	615	673	870	940
Channel Effective Wavelength (nm)						
Mean	414.4	499.5	612.0	666.9	863.5	937.7
Standard deviation	1.7	1.8	3.5	5.2	5.8	2.2
Minimum	409.1	496.4	605.9	656.0	845.7	926.6
Maximum	416.5	502.1	616.3	674.8	870.4	940.8
Rayleigh Optical Depth (1013.25 mb)						
Mean	0.311	0.144	0.063	0.044	0.0157	0.0112
Standard deviation	0.005	0.002	0.001	0.001	0.0004	0.0001
Minimum	0.306	0.141	0.061	0.042	0.0152	0.0111
Maximum	0.328	0.148	0.066	0.048	0.0170	0.0118
NO_2 Optical Depth (1 DU)						
Mean	0.0158	0.0063	0.0007	0.0002	0.0000	0.0000
Standard deviation	0.0001	0.0002	0.0001	0.0000	0.0000	0.0000
Minimum	0.0157	0.0060	0.0006	0.0001	0.0000	0.0000
Maximum	0.0162	0.0067	0.0009	0.0002	0.0000	0.0000
O_3 Optical Depth (300 DU)						
Mean	0.0000	0.0093	0.0366	0.0143	0.0005	0.0000
Standard deviation	0.0000	0.0009	0.0020	0.0016	0.0002	0.0000
Minimum	0.0000	0.0076	0.0343	0.0119	0.0003	0.0000
Maximum	0.0000	0.0106	0.0394	0.0178	0.0008	0.0000

head) spectral response may result in large systematic biases. To estimate, let us take ozone from a 615 nm channel, where its absorption is maximal. Assuming that the true amount of ozone is 300 DU corresponding to an OD of 0.0366 (mean value among our heads), the standard deviation in OD of 0.002 corresponds to 16 DU. In a more extreme situation, when a measurement is made with a head, which has a response of 0.0343 ozone OD for 300 DU, and the analysis assumes 0.0394 for 300 DU, the ozone amount will be underestimated by unacceptably large 40 DU.

3. Detection of Instrument Misalignment

Here we apply the term "misalignment" to any situation where the actual position of the instrument's shadow band differs from the nominal position calculated for given Sun angles. Misalignment can be caused by any combination of clock drift, error in instrument orientation (the axis pointing not strictly to the south in the northern hemisphere), and tilt. These technical inaccuracies may prevent the shadow band from shading the diffuser completely during the blocked measurement. The data collected during periods of serious misalignment are lost beyond recovery. Thus, timely detection of this problem is important, as well as an ability to filter already collected data to discard affected parts. A serious misalignment problem is easily recognized by visually inspecting plots of the direct normal and diffuse horizontal irradiances produced by the instrument. Figure 6 (top left) shows an illustrative example: SGP MFRSR data from the E3 extended facility for 13 November 2000. We see that misalignment induces oscillation in both direct and diffuse measurements and, consequently, in the derived OD. The top right panel shows a detailed view of these oscillations in 870 nm AOD, taken at some 500 s interval in the middle of the day. The actual measurements depicted by diamonds are made every 20 s, thus the period of the oscillations alternates between 100 and 120 s (five and six data points). Note that if the recorded MFRSR measurements are averages over several samples the picture will be different and the analysis presented in this section cannot be applied directly. The explanation of this effect is the following: the MFRSR shadow band rotates in descret steps, and it takes 800 steps to complete one full revolution. Since there are 360° in a full rotation, each step is 360°/800 = 0.45°. The Sun moves 1° of hour angle in 4 min; therefore, every 20 s it moves 0.0833°. The motor will not take a full 0.45° step until the Sun moves 0.45°; therefore, it takes between five and six 20 s measurement samples before it steps. This means that if the Sun is partially shining on the diffuser in the beginning of the five to six sample cycle (see Fig. 7 for a schematic) it will progressively expose more and more diffuser until it takes a full step, which will bring it back to near the position it started resulting in a repeating pattern with 100–120 s period.

The well-established periodicity of artificial oscillations in AOD due to misalignment suggests that a Fourier transform related technique may be used to automatically detect the problem. We designed such

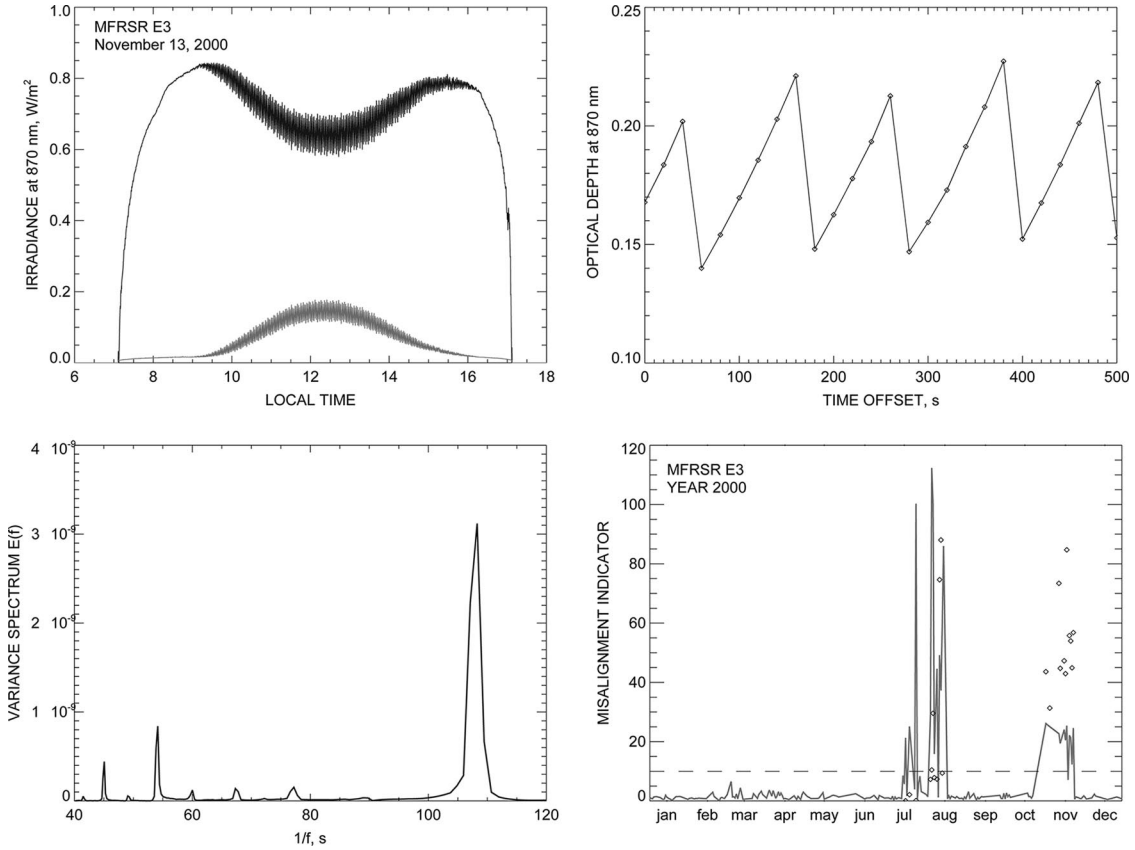

Fig. 6. Detection of MFRSR misalignment problem. Top left: direct (black) and diffuse (gray) irradiances from E3 MFRSR for 13 November 2000. Top right: artificial oscillations in 870 nm AOD from some interval in the middle of that day. Bottom left: variance spectrum of 870 nm AOD as function of inverse frequency in the range containing artificial "spectral lines" caused by the misalignment. Bottom right: time series of misalignment indicator Eq. (30) values for E3 in 2000. The diamonds indicate the severity of the problem (I_2 in arbitrary units) for the affected days.

a technique based on the variance ("energy") spectrum $E(f)$ of the AOD time series $\tau(t)$ $(0 \le t \le T)$ defined as

$$E(f) = \frac{2}{T}|\hat{\tau}(f)|^2, \quad f > 0, \tag{27}$$

where f is the frequency variable $(-\infty < f < \infty)$, and $\hat{\tau}(f)$ is the Fourier transform of $\tau(t)$. We use the discrete fast Fourier transform (FFT) in our computations. $E(f)$ is related to the variance of $\tau(t)$:

$$\mathrm{var}(\tau) = \frac{1}{T}\int_0^T |\tau(t) - \bar{\tau}|^2 \mathrm{d}t = \int_0^\infty E(f)\mathrm{d}f, \tag{28}$$

where the overbar denotes the average in t over T. Thus, the variance spectrum contains information about the way the total variance of the time series is divided between different frequencies. If a time series has a specific frequency f_0 dominating its variability, $E(f)$ will have a sharp maximum ("spectral line") at f_0.

The part of the variance spectrum for the 870 nm time series from 13 November is shown in Fig. 6 (bottom left). This is the only part of the spectrum, which contains spectral lines. The spectrum is plotted versus the inverse frequency to better relate it to the periodicity in Fig. 6 (top right). Indeed, the main spectral line in the spectrum is centered at $1/f_0 = 108$ s, which is between 100 and 120 s periods in the time series oscillations. Two more lines corresponding to 54 and 45 s inverse frequencies probably reflect the irregular shape of the AOD oscillations. Needless to say, all of these lines would not be present in the spectrum if the instrument was accurately aligned.

While the spectral signature of misalignment is quite sharp and well defined on a clear day, the presence of thin clouds can make the spectrum much noisier. The spectrum in this case may consist of many strong lines, which make it difficult to single out the misalignment signature. An application of the variability-based cloud screening algorithm [18] to the data is problematic for these purposes, since it screens out most misalignment artifacts as clouds. To resolve this problem we adopted a less restrictive cloud screening with a threshold of $\varepsilon = 0.01$ rather than the standard 2×10^{-4}. This screens out most variable broken clouds, while preserving clear sky intervals affected by misalignment. Since the Fourier transform is not supposed to be applied to data with

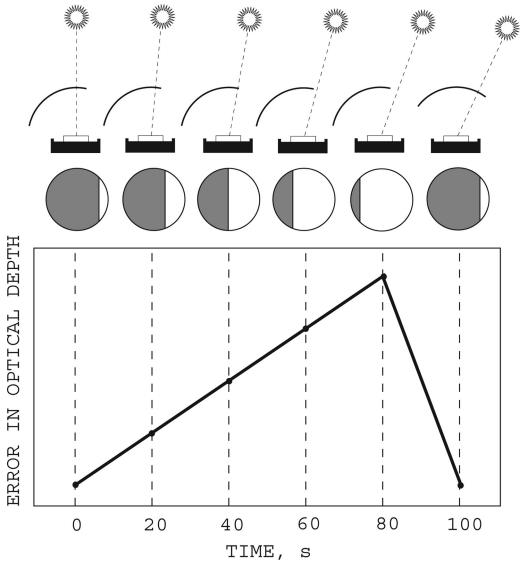

Fig. 7. Schematic of the mechanism of creating oscillations in OD by the instrument's misalignment. The top row of pictures shows the MFRSR diffuser and the shadow band partially blocking the Sun throughout the 100 s cycle of operation. The middle row shows the corresponding shading of the diffuser. All Sun and shadowband angles, as well as the shading degrees, are not to scale. The bottom plot presents the corresponding artificial OD introduced by this process [similar to that in Fig. 6 (top right)].

gaps, we select the longest available clear interval for the day, which should not be shorter than 200 data points (~1 h).

To characterize the main misalignment spectral line we select three subsequent intervals in the frequency domain between the four points $f_1 < f_2 < f_3 < f_4$ corresponding to $1/f$ values of 115, 110, 105, and 100 s, respectively. The interval between f_2 and f_3 contains the line maximum, while the other two intervals $[f_1, f_2]$ and $[f_3, f_4]$ are in the line's wings. Then, we define the three characteristic variance integrals:

$$I_i = \langle E(f) \rangle_{[f_i f_{i+1}]} = \frac{1}{f_{i+1} - f_i} \int_{f_i}^{f_{i+1}} E(f) \mathrm{d}f, \qquad (29)$$

$i = 1, 2, 3$, which are the averages of $E(f)$ over the respective intervals. After this the following two measures of misalignment can be defined: the first is the line's "significance,"

$$h = \frac{2I_2}{I_1 + I_3}, \qquad (30)$$

which describes the clarity of the line (the ratio between its peak and wings). h is a "misalignment indicator," which points to the problem even if it is negligibly small. Thus, we need a second parameter reflecting the severity of the problem, i.e., how much variance is concentrated in the misalignment frequency. This parameter is the line's "strength," which is simply I_2, and may be normalized by a convenient factor.

The detection method described above was applied to year-long MFRSR datasets from several SGP extended facilities for the year 2000. The data identified as affected by misalignment were then visually examined, and the problems were tracked to their starting and ending points. The sample time series of h values for E3 MFRSR is presented in Fig. 6 (bottom right). Two periods of misalignment are clearly seen, each about a month long: the first is in July and August, the other is in November (from where we took our example). Visual examination of the data suggested that $h = 10$ (depicted by a dashed line in the plot) is a reasonable threshold value to generate an alert. Indeed, the h values from unaffected intervals in the plot are below this value. We discovered that the residual cloud variability may create large I_2 but not h (actually, it can even decrease h). The arbitrarily scaled values of I_2 for the affected days are shown in Fig. 6 (bottom right) by diamonds. It is seen that even a slight problem (as, e.g., in July and the beginning of August), which is practically insignificant for measurements and retrievals, may result in a large h. This is a rather good sign, since misalignment has a tendency to develop over time; thus early detection is beneficial. The Central Facility MFRSRs (E13 and C1), which are probably the best looked after in the network, showed no signs of misalignment in 2000. E1 MFRSR was affected by the misalignment more or less continuously throughout the first half of the year, which then seems to be fixed.

4. Discussion

It was shown [19,20] that MFRSR measurements of spectral AOD agree with those by AERONET within the measurement accuracy. A companion study [21] shows similar agreement between MFRSR and AERONET's almucantar scan retrievals not only for total AOD, but also for fine and coarse mode AOD, and fine mode effective radius. This demonstrates that MFRSR measurements constitute a valuable global dataset with contributions from hundreds of instruments deployed worldwide. The highest concentration of MFRSRs is in the United States where most of them are associated with networks operated by the DOE ARM Program, USDA UV-B Monitoring and Research Program, NOAA SURFRAD Network, and NASA SIRN.

The ruggedness, automatic operation, and relatively low cost makes the MFRSR attractive to a growing number of researchers that are often not affiliated with major networks. This emphasizes the importance of keeping instrument mentors and data users aware of technical problems the instruments may encounter during operation and the impact of these problems on measurements. The study presented here addresses some issues that have not been addressed in other studies, and suggests ways to detect and correct them.

Unlike the tracking Sun photometer, a shadowband instrument is not able to adjust its focus on the

Sun. Thus, the precision of instrument alignment is essential for optimum measurement quality. Alignment includes the instrument orientation, both horizontal (pointing to the south in the northern hemisphere) and vertical (tilt), and clock timing of shadow-band operation. Undoubtedly the worst operational malfunction is severe misalignment, where the shadow band only partially covers the diffuser in the "block" measurement position for a large portion of the day. This results in a permanent loss of data. If not detected and corrected, this problem may persist for months. Misalignment in a developed state can easily be detected by visual inspection of a MFRSR measurement's time series on a relatively clear day (e.g., Fig. 6, top left). Nevertheless, instrument mentors need an automatic alert system that (a) can warn them in the early stages of the problem when data are still acceptable, and (b) does not require routine visual evaluation of the data, which is especially important for large networks. In this paper we suggest a computationally simple procedure that is able to automatically track the misalignment problem even when it may be difficult to detect visually. This method is based on discrete fast Fourier transform (FFT) of OD time series. FFT is a widely used procedure implemented in most major programing languages.

Another, typically less severe, problem is instrument tilt that may arise from an unstable instrument platform. If the tilt is not severe enough to produce a major misalignment as described above, it may be quite difficult to detect from the data. Fortunately, the errors in AOD induced by a 1° tilt are of the order of 0.01, comparable to calibration accuracy, although larger tilts may notably bias the measurements. Once tilt magnitude and direction are determined, data can be corrected according to Eq. (20). Definitive tilt detection and estimation of its magnitude remains to be made through the instrument leveling check. We suggest a simple regression-based procedure allowing us to detect a tilt from the data in some cases. This procedure requires a colocated tracking Sun photometer (e.g., CIMEL), and is limited to tilts in the west–east direction. A relative tilt of two colocated shadow-band instruments can be determined in a similar manner. However, while this can call a mentor's attention to both instruments, it is impossible to determine from the data which instrument (or both) is tilted.

We have examined a variety of spectral responses from a number of MFRSR heads and conclude that, except for water vapor retrievals, replacement of one set of head-specific parameters with another does not generally cause an error in OD that exceeds the measurement accuracy. However, such misplacement (or poor determination of MFRSR spectral response) may cause a significant error in ozone column retrievals, which may well exceed the accuracy of available satellite measurements by a Total Ozone Mapping Spectrometer (TOMS) or Global Ozone Monitoring Experiment (GOME). Thus, we do not recommend ozone retrieval to be a part of MFRSR data analysis unless the instrument's spectral response is well known.

We also examined the history of changes in angular responses of two MFRSR heads deployed at the ARM North Slope of Alaska site in 2002–2006. This examination demonstrated, that while these changes normally do not result in OD errors larger than the calibration accuracy, they may indicate a faulty head. This underlines the necessity to check MFRSR angular responses regularly.

We also addressed a problem that is not specifically instrumental, but is caused by a bug in manufacturer-supplied software for converting the MFRSR binary output into calibrated irradiances stored in ASCII files. This is the erroneous correction of the direct normal irradiance for nighttime offsets (black counts), which should not be made, since in a shadow-band measurement scheme the direct irradiance is a difference measurement, in which the offsets are canceled. If the erroneously applied offsets are positive, they can be observed in direct normal data in absence of direct sunlight (early dawn, late dusk, or a completely overcast day). They also can be calculated using the information in the manufacturer-supplied calibration file, which the user can also check to see if the offsets are applied properly. The magnitude of the offset impact on OD retrieval is exponential with total OD (including Rayleigh and ozone contributions). This calls special attention to the 415 nm channel, which has the largest OD. It appears that, for typical OD values and the offsets usually encountered in SGP dataset, the impact on OD at 415 nm is $\sim$0.02, while it is below 0.01 for the rest of MFRSR channels. This is close to the calibration accuracy of the instrument and can therefore be tolerated. However, in situations when AOD at 870 nm is higher than 0.2, the offset problem may cause serious errors, and the data must be corrected for further analysis.

We conclude that, despite possible problems, the MFRSR remains an important instrument capable of making measurements as accurately as tracking Sun photometers such as CIMEL. However, MFRSR users should be aware of instrumental problems they may encounter and of ways to detect and correct them.

This research was supported by the Office of Biological and Environmental Research of the U.S. Department of Energy as part of the Atmospheric Radiation Measurement Program. We thank J. Schmelzer for useful discussions and for technical data used in this paper and R. Wagener for his effort to maintain the AERONET site at SGP's Central Facility.

References

1. B. Holben, T. F. Eck, I. Slutsker, D. Tanre, J. P. Buis, A. Setzer, E. Vermote, J. A. Reagan, Y. Kaufman, T. Nakajima, F. Lavenu, I. Jankowiak, and A. Smirnov, "AERONET—A federated instrument network and data archive for aerosol characterization," Remote Sens. Environ. **66,** 1–16 (1998).
2. L. Harrison, J. Michalsky, and J. Berndt, "Automated multifilter shadow-band radiometer: instrument for optical depth

and radiation measurement," Appl. Opt. **33,** 5118–5125 (1994).
3. J. J. Michalsky, F. A. Schlemmer, W. E. Berkheiser, J. L. Berndt, L. C. Harrison, N. S. Laulainen, N. R. Larson, and J. C. Barnard, "Multiyear measurements of aerosol optical depth in the Atmospheric Radiation Measurement and Quantitative Links Programs," J. Geophys. Res. **106,** 12099–12107 (2001).
4. L. Harrison, M. Beauharnois, J. Berndt, P. Kiedron, J. Michalsky, and Q. L. Min, "The rotating shadowband spectroradiometer (RSS) at SGP," Geophys. Res. Lett. **26,** 1715–1718 (1999).
5. P. W. Kiedron, L. Harrison, J. J. Michalsky, J. Schlemmer, and J. L. Berndt, "Data and signal processing of rotating shadowband spectroradiometer (RSS) data," Proc. SPIE **4815,** 51–57 (2002).
6. P. W. Kiedron and J. J. Michalsky, "Measurement errors in diffuse irradiance with non-Lambertian radiometers," Int. J. Remote Sens. **24,** 237–247 (2003).
7. T. P. Ackerman and G. Stokes, "The Atmospheric Radiation Measurement Program," Phys. Today **56**(1), 38–44 (2003).
8. D. S. Bigelow, J. R. Slusser, A. F. Beaubien, and J. H. Gibson, "The USDA Ultraviolet Radiation Monitoring Program," Bull. Am. Meteorol. Soc. **79,** 601–615 (1998).
9. J. A. Augustine, G. B. Hodges, C. R. Cornwall, J. J. Michalsky, and C. I. Medina, "An update on SURFRAD—the GCOS Surface Radiation Budget Network for the continental United States," J. Atmos. Oceanic Technol. **22,** 1460–1472 (2005).
10. A. Ohmura, H. Gilgen, H. Hegner, G. Muller, M. Wild, E. G. Dutton, B. Forgan, C. Frohlich, R. Philipona, A. Heimo, G. Konig-Langlo, B. McArthur, R. Pinker, C. H. Whitlock, and K. Dehne, "Baseline Surface Radiation Network (BSRN/WCRP): new precision radiometry for climate research," Bull. Am. Meteorol. Soc. **79,** 2115–2136 (1998).
11. R. M. Mitchell and B. W. Forgan, "Aerosol measurement in the Australian Outback: intercomparison of Sun photometers," J. Atmos. Oceanic Tech. **20,** 54–66 (2003).
12. Q. Min, E. Joseph, and M. Duan, "Retrievals of thin cloud optical depth from a multifilter rotating shadowband radiometer," J. Geophys. Res. **109,** D02201, doi:10.1029/2003JD003964 (2004).
13. Q. Min and M. Duan, "Simultaneously retrieving cloud optical depth and effective radius for optically thin clouds," J. Geophys. Res. **110,** D21201, doi:10.1029/2005JD006136 (2005).
14. F. Kasten and A. T. Young, "Revised optical air mass tables and approximation formula," Appl. Opt. **28,** 4735–4738 (1989).
15. L. Harrison, P. Kiedron, J. Berndt, and J. Schlemmer, "Extraterrestrial solar spectrum 360–1050 nm from rotating shadowband spectroradiometer measurements at the Southern Great Plains (ARM) site," J. Geophys. Res. **108,** 4424, doi:10.1029/2001JD001311 (2003).
16. L. Harrison and J. Michalsky, "Objective algorithms for the retrieval of optical depths from ground-based measurements," Appl. Opt. **33,** 5126–5132 (1994).
17. J. J. Michalsky, L. C. Harrison, and W. E. Berkheiser, "Cosine response characteristics of some radiometric and photometric sensors," Sol. Energy **54,** 397–402 (1995).
18. M. Alexandrov, A. Marshak, B. Cairns, A. Lacis, and B. Carlson, "Automated cloud screening algorithm for MFRSR data," Geophys. Res. Lett. **31,** L04118, doi:10.1029/2003GL019105 (2004).
19. M. Alexandrov, A. Lacis, B. Carlson, and B. Cairns, "Remote sensing of atmospheric aerosols and trace gases by means of Multi-Filter Rotating Shadow-band Radiometer. Part I: retrieval algorithm," J. Atmos. Sci. **59,** 524–543 (2002).
20. M. Alexandrov, B. Carlson, A. Lacis, and B. Cairns, "Separation of fine and coarse aerosol modes in MFRSR data sets," J. Geophys. Res. **110,** D13204, doi:10.1029/2004JD005226 (2005).
21. M. Alexandrov, A. Lacis, B. Carlson, and B. Cairns, "Characterization of atmospheric aerosols using MFRSR measurements" (submitted to J. Geophys. Res.).